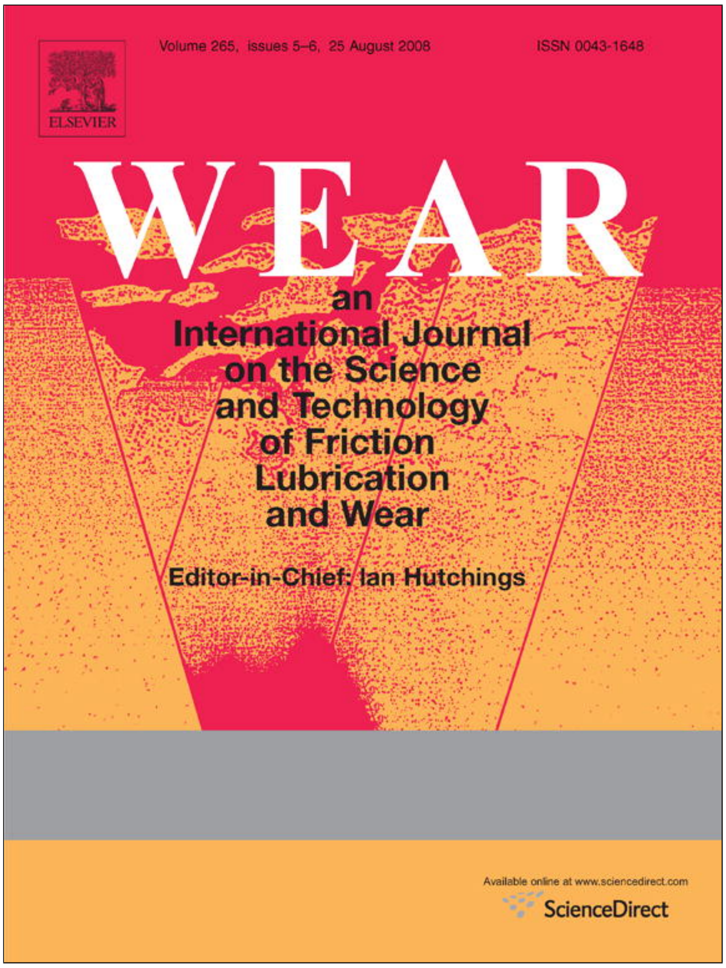
Volume 265, issues 5–6, 25 August 2008
ISSN 0043-1648
ELSEVIER
WEAR
an
International Journal
on the Science
and Technology
of Friction
Lubrication
and Wear
Editor-in-Chief: Ian Hutchings
Available online at www.sciencedirect.com
ScienceDirect

Available online at www.sciencedirect.com
ScienceDirect
Wear 265 (2008) 741–755
WEAR
www.elsevier.com/locate/wear

Deposition and characterization of hybrid filtered arc/magnetron multilayer nanocomposite cermet coatings for advanced tribological applications

V.I. Gorokovsky [a], C. Bowman [a,*], P.E. Gannon [a,b], D. VanVorous [a], A.A. Voevodin [c], C. Muratore [c], Y.S. Kang [c], J.J. Hu [c]

[a] *Arcomac Surface Engineering, LLC, 151 Evergreen Drive, Ste D. Bozeman, MT 59715, United States*
[b] *Montana State University, United States*
[c] *Air Force Research Laboratory, United States*

Received 31 October 2006; received in revised form 13 December 2007; accepted 9 January 2008
Available online 4 March 2008

Abstract

The demand for low-friction, wear and corrosion resistant components, which operate under severe conditions, has directed attention to advanced surface engineering technologies. The large area filtered arc deposition (LAFAD) process has demonstrated atomically smooth coatings at high deposition rates over large surface areas. In addition to the inherent advantages of conventional filtered arc technology (superhardness, improved adhesion, low defect density), the LAFAD technology allows functionally graded, multilayer, and nanocomposite architectures of multi-elemental coatings via electro-magnetic mixing of two plasma flows composed of different metal vapor ion compositions. Further advancement is realized through a combinatorial process using a hybrid filtered arc–magnetron technique to deposit multilayer nanocomposite TiCrN + TiBC cermet coatings. Multiple TiCrN + TiBC coating architectures were reviewed for their ability to provide wear resistance for Pyrowear 675 and M50 steels used in aerospace bearing and gear applications. Coating properties were characterized by a variety of methods including SEM/EDS, HRTEM, and XRD. Wear results were obtained for high contact stress boundary lubricated sliding and advanced bearing simulation testing for wear performance under oil-off operating conditions. The best coating candidates demonstrated order of magnitude increases in resistance to sliding wear, and extended low friction operation during simulated oil-off events. Coating failure mechanisms were brittle in nature and suggestions are presented for the further optimization of TiCrN + TiBC coating architectures.

Keywords: Filtered arc; Magnetron; Nanocomposite; Aerospace; Oil-off event; Sliding wear

1. Introduction

Future generations of aircraft engines and transmissions demand high-temperature gear and bearing materials having superhard, corrosion and wear resistant surfaces, while maintaining desired core properties, e.g., excellent fracture toughness, fatigue life, impact resistance and ductility. The development of new materials to meet these requirements is costly and slow due to the safety-critical nature of the application and the limited selection of metallurgically stable (thermodynamically favored) metal alloys. Recently, attention has been directed toward surface engineering for gear and bearing materials to reduce wear, increase corrosion resistance, and provide a thermal barrier to the core material all over wide temperature and engine duty cycle ranges while maintaining or improving fatigue life.

The tribological properties of any surface engineered gear or bearing material should be viewed as a system. A key requirement for such a surface engineered system would be to secure both corrosion and tribological performance, while satisfying the case/core/coating compatibility condition [1]. Conventional coatings, such as thin dense chrome, not only fail to perform to this specification but also are subjected to restricted usage due to hazardous material requirements [2]. Several approaches for surface engineering of heavily loaded friction pair components have been developed. They employ surface diffusion saturation

* Corresponding author. Tel.: +1 406 522 7620; fax: +1 406 522 7617.
E-mail address: cbowman@arcomac.com (C. Bowman).

0043-1648/$ – see front matter © 2008 Elsevier B.V. All rights reserved.
doi:10.1016/j.wear.2008.01.003

treatment (ion-nitriding, carburizing), hard composite electroplating coatings, PVD and CVD cermet coatings of different compositions and architectures, as well as, duplex treatment: coating deposition over a previously hardened surface layer. Sputter deposition of boron carbide coating is an established PVD technology used for improvement of wear and tribological properties of automotive components, such as transmission gears and bearings [3]. Boron carbide is the third hardest known material, after diamond and cBN, but its brittleness and low-fracture toughness often prevent its use in high load contact applications. Another candidate coating having near diamond hardness and low friction is hydrogen-free DLC deposited by filtered cathodic arc deposition. However, this material also exhibits relatively low-fracture toughness at high loads [4].

Several approaches are under development to overcome the characteristic brittleness of hard coatings. These include deposition of multi-component coatings with layered architectures on both micro- and nano-metric scales. Various elemental additions and coating structure modifications are being investigated to form optimized nanocomposite cermet materials [5–8]. Metal-doped DLC coatings have shown reduced wear rates compared with metal-free DLC coatings prepared by glow discharge techniques [9]. Further addition of carbon, silicon and/or nitrogen to B–C and Ti–B–C coatings was found to improve fracture toughness and wear resistance via improved lattice bonding, which reduces the characteristic brittleness of these ceramics [2,5–7,9]. Recently developed nanocomposite cermet coatings demonstrate dramatic improvement in coating hardness, up to superhard levels >40 GPa. It is suggested that nanocomposites consisting of nanocrystals of carbides, nitrides or borides embedded into an amorphous matrix of doped carbon, silicon nitride, boron nitrides or similar materials improve hardness by inhibiting dislocation movement (Hall–Petch mechanism) [6–8,10–14]. Nanocomposite coatings with nanocrystalline/amorphous structures and functionally gradient metal–ceramic interfaces on steel substrates have been designed to provide supertough characteristics and the capability to withstand high contact loads of gear and bearing materials in aerospace systems [11–13,15–19].

Coating deposition processes and equipment capable of multilayer, substructured, multi-element nanocomposite coating deposition must have several different metal vapor or sputtering sources providing highly ionized and activated metal vapor plasma. Elimination of coating macroparticles and growth defects is critically important to achieve high performance of corrosion and wear resistive coatings [20–22]. The challenge is to develop a method which provides high deposition rates, coatings with high density, fine-grained microstructure, improved adherence to the substrate, and high toughness. The deposition technique should allow tailoring of the microstructure and interface properties, be robust, cost effective, provide desirable surface profile and compatibility throughout the entire core/case/coating system.

Arcomac's large area filtered arc deposition (LAFAD) technology generates a fully ionized, macroparticle-free metal vapor in a highly activated and reactive gas plasma environment [23,24]. A recent advance in this technology is the development of the hybrid filtered arc deposition/unbalanced-magnetron sputtering (FAD/UBM) surface engineering process, which permits control of metal vapor plasma streams from different metal vapor and sputtering sources in single vapor and multiple co-vapor deposition modes [25,26]. The hybrid combination of FAD/UBM increases the metal ion flux toward the substrate via filtered arc plasma, while maintaining the flux of neutral atoms generated by magnetron sputtering. This approach is similar to the hybrid magnetron sputtering-pulse laser deposition (MSPLD) process described in Refs. [15,16], which uses pulse laser plasma in combination with magnetron sputtering. The MSPLD technology provides multiple vapor plasma with high ionization rate; however, it is limited in scale-up capabilities.

In this paper, hybrid FAD/UBM surface engineering processes are investigated via the deposition of Ti–Cr–B–C–N containing multilayer nanocomposite cermet coatings for highly loaded tribological applications operating in corrosive environments.

2. Experimental details

2.1. Hybrid FAD–UBM coating deposition process and coating design

Arcomac's filtered arc plasma source ion deposition (FAPSID-700) surface engineering system was used in this study to perform hybrid FAD–UBM coating depositions. The FAPSID-700 employs two LAFAD-500 dual filtered cathodic arc sources, two unbalanced magnetrons, as well as, electron beam physical vapor deposition (EBPVD) and thermal evaporation sources in one universal vacuum chamber layout (Fig. 1) [25,26]. The LAFAD plasma source magnetic deflecting system allows bending of the metal vapor plasma jets at 90 °C toward substrates to be coated, which yields 100% ionized metal vapor plasma flow at the LAFAD source exit and near 50% ionized gaseous plasma in the coating chamber. When the magnetic deflecting subsystem is turned off the LAFAD source can be used in a gas ionization mode as a powerful electron emitter. In this mode the auxiliary arc discharge is ignited between the primary cathodes of the LAFAD source and an auxiliary anode located in the coating chamber (Fig. 1).

For simplicity the basic coating architecture used in this work is on occasion referred to as TiCrN + TiBC to emphasize the concept of a two segment coating approach, with each segment providing a primary function. The concept of the two segment approach is that the bottom TiCrN segment functions as a corrosion resistant and elastic support layer for the hard TiBC top segment coating which in turn functions as a wear resistant layer.

In detail, the coating is actually very complex as shown in Fig. 2. The bottom segment coating is a multilayer TiCr metallic TiCrN nitride architecture denoted as TiCr–TiCrN. For the TiCr–TiCrN deposition, the LAFAD source was equipped with titanium and chromium targets, installed opposite each other in the primary cathodic arc sources of the LAFAD plasma source (see Fig. 1). In this process the substrates to be coated are installed on a rotating substrate holding platform, and subjected in turn to titanium and chromium metal vapor plasma

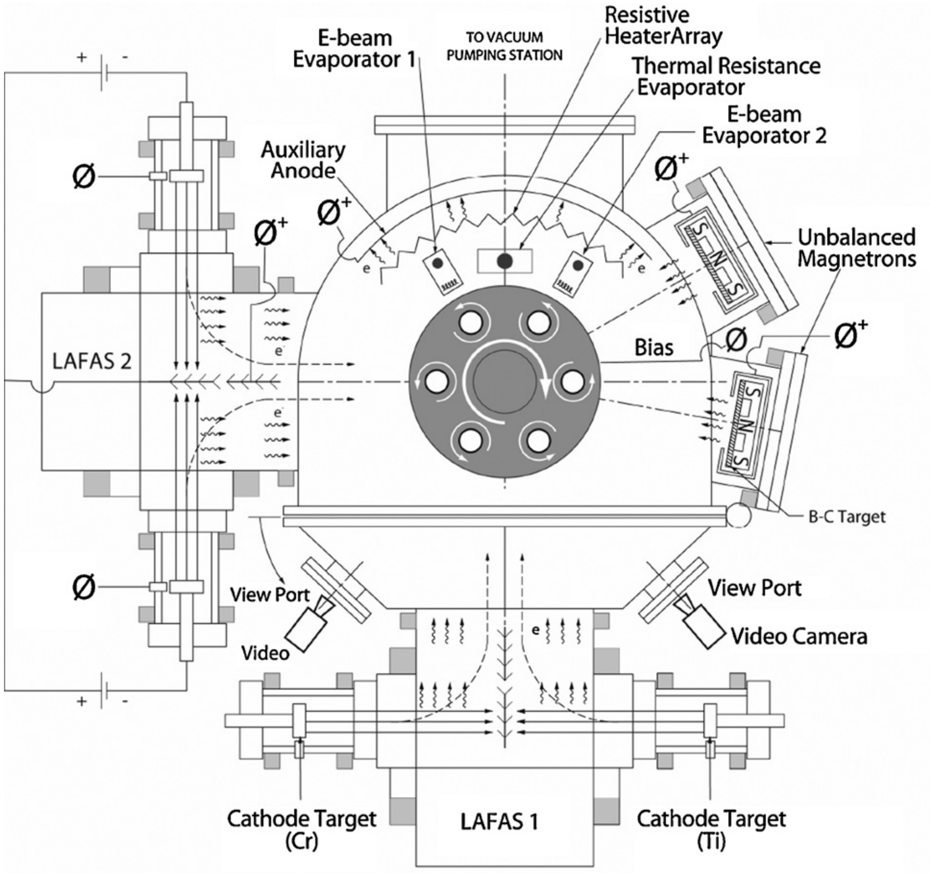

Fig. 1. Schematic illustration of Arcomac Surface Engineering FAPSID™ surface engineering system. This system utilizes the Large Area Filtered Arc Sources (LAFAS) in a Universal Hybrid Layout with conventional PVD sources: top view.

flows resulting in a nano-layering of Ti and Cr with a ∼3 nm period [26–29]. This nano-layer structure is present throughout the multilayer TiCr–TiCrN structure, which has ∼400 nm bi-layers comprised of a ∼100 nm TiCr layer and a ∼300 nm TiCrN layer. Typical process parameters for the LAFAD bottom segment multilayer TiCr–TiCrN coating deposition process can be found in Ref. [26]. A gradient transition was produced at the end of bottom segment TiCr–TiCrN deposition process to facilitate bonding with the top segment coating. Methane gas was gradually added to the nitrogen, raising the methane concentration from 0% to 40% over an elapsed time of 40 min, which resulted in the formation of a 0.5-μm thick gradient TiCrCN carbonitride layer.

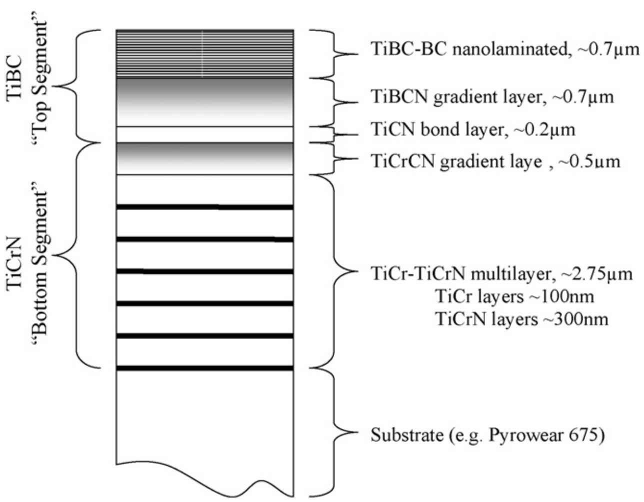

Fig. 2. TiCrN + TiBC coating schematic defining the general "bottom" and "top" segments (left side of schematic), and the detailed architecture of each coating segment (right side of schematic).

To deposit the top segment of the coating architecture the chromium target of LAFAD plasma source was replaced with a titanium target for the TiBC coating deposition process. TiBC is used to denote the top coating segment in general, as the actual coating architecture is quite complex. The TiBC top coating segment starts with a thin TiCN layer (∼0.2 μm) followed by a gradient TiBCN layer (∼0.7 μm) by continuous co-deposition of titanium vapor plasma generated by the LAFAD source and sputtered B_4C vapor generated by two UBM sources. At the end of the TiBCN deposition stage, the nitrogen flowrate was gradually reduced to zero and gas composition was changed to Ar (∼60 sccm) + CH_4 (∼4 sccm) at 0.1 Pa for deposition of the TiBC top coating segment, for a duration of 2 h. At this stage of the process, Ti content modulation was established by periodically turning off the LAFAD plasma source magnetic deflecting coils (magnetic shuttering mode). The number of bi-periods in the top coating segment architecture can be estimated as: $N = t/(t_{on} + t_{off})$, where t is total deposition time, t_{on} and t_{off} are periods of time when deflecting magnetic system of the LAFAD source is ON and OFF, respectively. The titanium flux cannot be fully interrupted in this process due to some titanium re-sputtering from magnetron targets, even though the LAFAD plasma source is magnetically shuttered. This approach allows control of Ti content modulation across the top coating segment. Using the magnetic shuttering technique with different t_{on}/t_{off} periodic ratios, four different Ti content modulation processes were studied: 5 s/15 s, 5 s/25 s, 5 s/55 s, and 0 s/60 s (Ti off process). This can be alternatively described as 25%, 17%, 8%, and 0% LAFAD Ti vapor plasma source duty cycle. As a result the general TiBC designation can be specifically defined as nanolaminated TiBC–BC architecture due to the titanium modulation. This layer structure exhibits nanometer-sized bilayers composed of titanium-enriched sublayers followed by titanium-deficient sublayers. A detailed schematic of the TiBC top segment coating is shown in Fig. 2.

2.1.1. Substrate identification

Coatings were deposited on case carburized Pyrowear 675, and through-hardened M50. Pyrowear 675 substrate material core properties were tested at ASTM grain size of 5–8, delta ferrite content of 2–5%, and core hardness of HRC 43–45. Case hardness was measured at HRC 63–65 and 13 GPa by nanoindentation at a depth of 3 μm. Pyrowear 675 samples were ground and lapped to an average roughness (R_a) of $R_a = 0.5$ μin. (13 nm), the lapping pattern was random and produced no visible lay direction. The M50 substrate material was certified AMS6491B, through hardened and double tempered to an average of HRC 64. The M50 samples were ground to $R_a = 3$–4 μin. (77–103 nm), with a random circular lay direction. Preliminary calibration of coatings was conducted on 440A stainless steel.

2.1.2. Coating characterization technique

Thin film X-ray diffraction (XRD) analysis was performed using a Rigaku Rotaflex X-ray diffractometer system with Cu Kα radiation incident at a fixed 4° angle of incidence. Samples were scanned from 20° to 100° of 2θ. A Jeol Model 6100 scanning electron microscope (SEM) equipped with a Noran energy dispersive X-ray spectrometer (EDS) was used for surface morphology assessments, cross-sectional imaging, and elemental analysis/mapping. Coating thickness was determined by the CALOtest™ spherical abrasion technique and optical micrometry to an accuracy of ±0.1 μm. Coating hardness and Young's modulus were measured by a MTS XP nanoindenter with a CSM module and Berkovich tip. Hardness and Young's modulus data for each indent were averaged over ∼150 data points over a range indentation depths of ∼5–10% of a given coating thickness to improve the accuracy of measurement and minimize any substrate effects, in addition 10 indent locations per sample were averaged to obtain statistical results. Effective Young's modulus $E^* = E/(1 - n^2)$, where n is Poisson's ratio of 0.2, and resistance to plastic deformation (H^3/E^{*2}) were calculated from obtained hardness (H) and Young's modulus (E) data as in Ref. [5]. Coating adhesion was assessed by the standard Rockwell indentation method using a 120° diamond indenter and a 1500-N load [30]. CSEM Revetest equipment was used for quantitative scratch test assessment of the coating adhesion/cohesion with the following test parameters: linear loading from 0 to 200 N, 100 N/min loading rate, 6.5 mm/min travel rate, 0.2 mm radius diamond tip. Coating failure was assessed by acoustic emission and tangential force monitoring during testing, and was confirmed by post-test back-scatter electron imaging (BEI) and SEM imaging.

Boundary lubricated sliding wear tests were conducted under simulated aerospace operating conditions of 3.0 GPa contact, ball (M50 uncoated, Grade 10 ball) on flat (P675 and M50 test coupons) geometry, at 0.36 m/s sliding velocity and 100% slip. Boundary lubrication was assumed for testing parameters which produced a ratio of the average surface roughness (R_a) to the calculated Couette-flow oil film thickness (h) of less than 1, $h/R_a < 1$. Mobil Jet 254 (MIL-Prf-23699) oil was used in testing at a flow rate of ∼0.1 cm^3/s. All tests were run for 4-min time, 85-m sliding distance, and then stopped.

A sliding wear oil-off testing protocol was developed between Arcomac and Wedeven Associates Inc. to evaluate the survivability of various contact pairs under simulated "oil-off event" turbine engine bearing operation conditions. Testing parameters were as follows: ball on flat contact, 2.1 GPa contact stress, 5.1 m/s entraining velocity, 200 °C operation temperature, Mil-PRF-23699 oil, and 3% slip. After 300 s of steady state operation the oil supply was shut off, the rise in the friction coefficient (μ) was monitored and, once a friction value of 0.15 (starting value was $\mu = 0.02$, elastohydrodynamic (EHD) mode) was reached the test was run for 200 s and then oil was reintroduced. Contact track wear was recorded on the ball and disc surfaces by surface profilometry and reflected light microscopy.

3. Results and discussion

Table 1 shows the relative elemental compositions of the deposited coatings as determined by EDS analysis. The TiCrN coating segment had slightly less Cr content than Ti, 25% Cr compared to 34% Ti, which was a result of the inherently lower deposition rate of chromium FAD targets. Carbon content shows up in the EDS data for the TiCrN coating due to the TiCrCN gradient transition layer (Fig. 2). Iron content was included in all measurements as a check to confirm no substrate interaction was occurring in the measurement. The effect of the magnetic shuttering on Ti modulation in the top segment TiBC architecture can also been seen, Ti content increases from 31% to 34% to 43% for the defined 5/55, 5/25, and 5/15 periodic ratios, respectively. The actual variation in Ti content between the 5/55, 5/25, and 5/15 periodic ratios is likely greater due to the fact that as the periodic ratio decreases the deposition rate of the Ti modulated layer decreases, resulting in an increasing chance that the EDS analysis volume is interacting with the Ti rich TiBCN preliminary layer. Ti content in the (Ti)BC 0/60 (Ti off) coating variation was measured at 15%, and explained by the same reasoning. Ti content in the TiBC 0/60 case can also be attributed to co-deposition of Ti from the FAD sources onto the UBM target surfaces; the data was considered appropriate as it relates more closely to commercial processing where UBM targets would not be replaced each run, and/or may not incorporate automated masking of the target surface during FAD only operation.

Table 1
Relative elemental composition (at.%) of coatings as determined by EDS

	Bottom segment	Top segment coating architecture Ti pulse deposition cycle t_{on}/t_{off} (ON[s]/OFF[s])			
	TiCrN	(Ti)BC (off)	TiBC (5/55)	TiBC (5/25)	TiBC (5/15)
Ti	34	15	31	34	43
B	–	64	50	46	41
C	8	19	18	20	14
N	33	–	–	–	–
Cr	25	–	–	–	–
Fe	–	1	–	–	1

The XRD analysis of the phase compositions of the FAD/UBM TiBC coatings with different Ti periodic ratios revealed the following three stoichiometric phases in the coatings: TiB_2, B_4C and TiC as shown in Fig. 3. For interpretation of these results, the ternary phase diagram of the Ti–B–C system was considered [44]. This diagram shows that the B_4C phase disappears in favor of a TiC phase as the Ti concentration increases. The diagram shows that TiB_2 appears to be the dominant crystalline phase, which co-exists throughout all possible elemental compositions either with TiC in the Ti-rich zone or with B_4C in the boron rich zone of the diagram. This phase composition exists in a wide range of temperatures from room temperature up to 1800 K [45–47]. This is a tendency which we also observed in the XRD spectra of our coatings [44]. More detailed studies using experimental phase diagrams and computational modeling, taking into consideration solid solutions and disordered crystalline phases, have shown that the ternary phases such as $(B_{12})_4Ti_{1.86}C_2$ solid solution ternary phase having a tetragonal boron structure described in [48], can appear only in the narrow border area between the $TiB_2 + TiC + C$ and $TiB_2 + B_4C + C$ zones [26,45–47]. During FAD/UBM deposition of TiBC coatings the substrates are periodically subjected

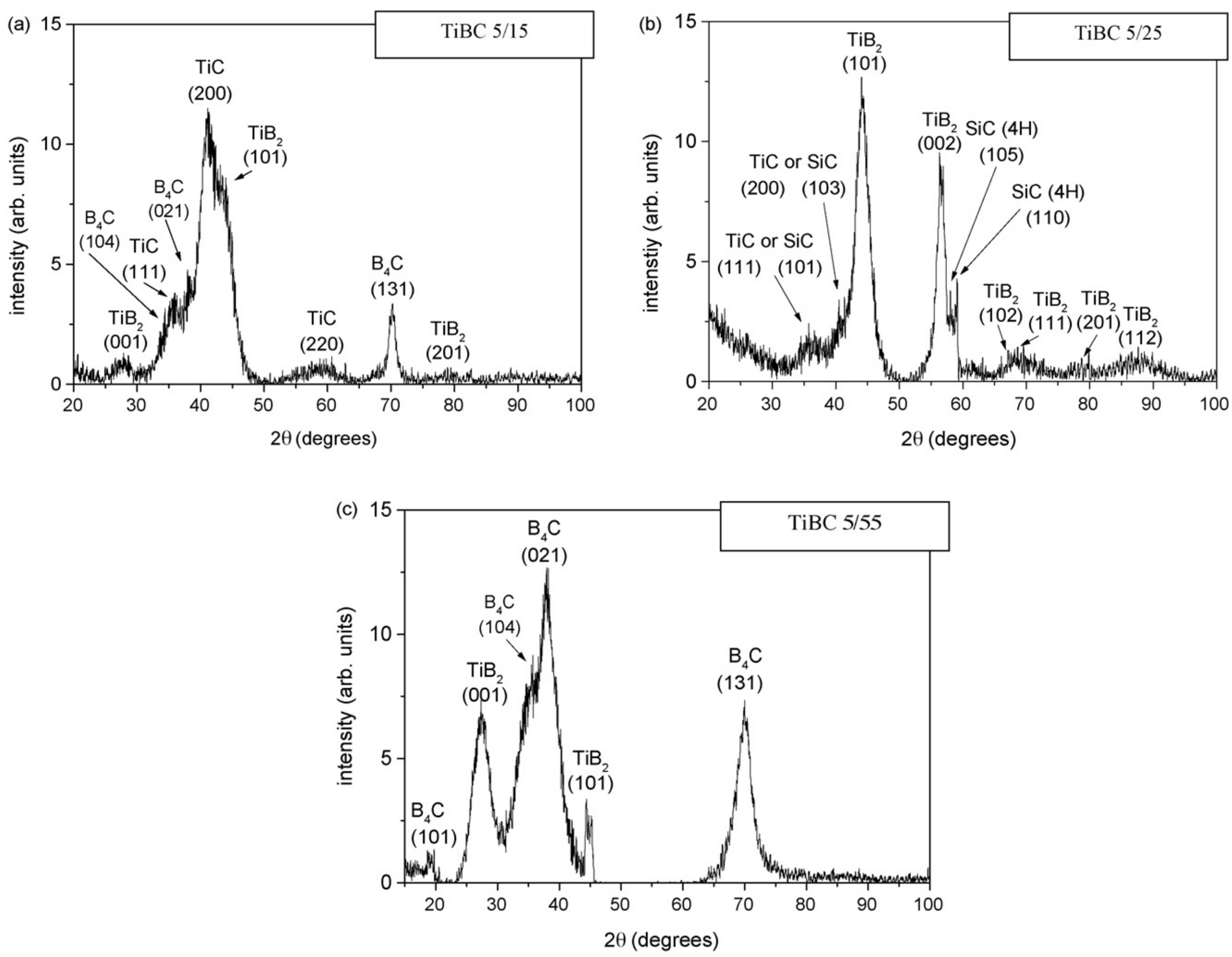

Fig. 3. XRD spectra of TiBC coatings with different Ti exposure ratios: (a) 5/15 ratio, (b) 5/25 ratio, and (c) 5/55 ratio.

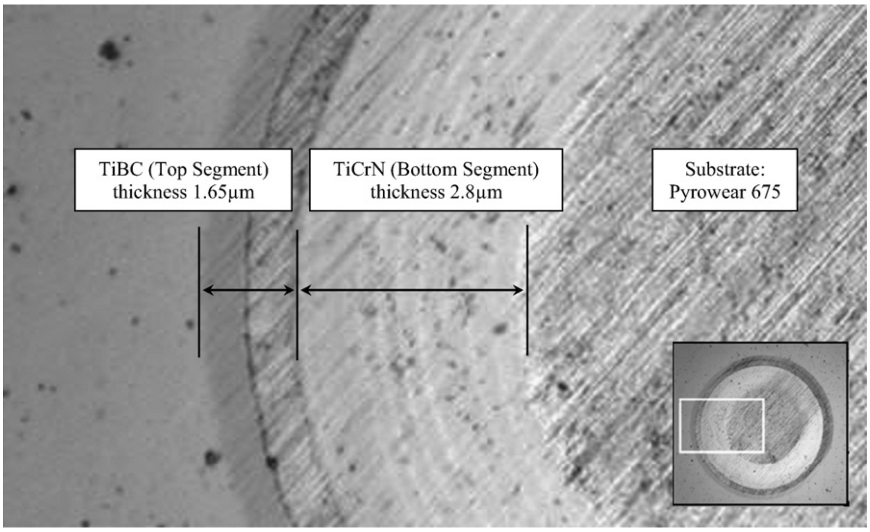

Fig. 4. Optical microscopy image of a CALOtest wear scar for coating #1 as deposited on Pyrowear 675. Inset image is at lower magnification and shows the zoom location of the primary image.

to an intense Ti plasma flow, resulting in a modulation of titanium concentration in the coatings (Fig. 2). According to the Ti–B–C phase diagram it is expected that TiB_2 + TiC + C will be deposited when the filtered arc titanium vapor plasma is added to the coating. When the magnetic shutter is closed the concentration of titanium in the TiBC coating is low resulting in a TiB_2 + B_4C + C phase composition. These results are in good agreement with results of XRD analysis (Fig. 3). It can be seen that as the Ti concentration increases (samples with 5/15 and 5/25 Ti exposure ratios) the coating consists of TiB_2 + TiC + B_4C composition. When the Ti concentration decreases (sample with 5/55 Ti exposure ratio) only TiB_2 and B_4C are seen in the XRD spectra of the coating. Therefore, by using magnetic shuttering it is possible to influence the coating phase composition in the FAD/UBM coating deposition process of TiBC coatings.

Table 2 shows the coating and substrate matrix produced for subsequent mechanical properties testing and tribological performance assessment. Preliminary development of the TiBC top segment architecture was conducted on 440A stainless steel substrates, and identified as coatings #3c, #4c, and #5c. The 5/25 TiBC and 0/60 (Ti)BC top segments were selected for full testing assessment and deposited as the complete top and bottom coating architecture on Pyrowear 675 and M50 substrates, and identified as coatings #1 and #2. A CALOtest^{TM} wear scar micrograph of coating #1 is shown in Fig. 4 as deposited on Pyrowear 675 with the two segment architecture clearly visible. The bottom segment multilayer architecture can be seen, as well as the delineation in the top segment as a result of the magnetic shuttering (further explained by HRTEM results discussed below). The TiCN + TiBCN layer deposited during the first 30 min of the top segment 2.5 h coating process comprises ~55% of the total segment thickness. This is a result of substantially greater deposition rate of continuous FAD/UBM operation during TiBCN deposition versus the lower deposition rate during magnetic shuttering FAD/UBM operation.

Table 2
Coating sample matrix for Pyrowear 675, M50 and 440A substrates

Coating code	Architecture thickness (μm)		Substrate(s)
	Bottom segment	Top segment	
#1	TiCrN (2.8)	0/60 (Ti)BC (1.6)	P675, M50
#2	TiCrN (2.5)	5/25 TiBC (1.5)	P675, M50
#3c	n/a	5/55 TiBC (1.8)	440A
#4c	n/a	5/25 TiBC (1.5)	440A
#5c	n/a	5/15 TiBC (1.8)	440A

Fig. 5 presents HRTEM micrographs of the 5/55 TiBC top segment coating deposited on a Si substrate. The initial TiCN layer (~0.2 μm) interfaces with the Si substrate, followed by a thicker TiBCN layer (~0.7 μm). The columnar structure of these layers is evident and is common for transition metal nitride coatings deposited by filtered arc and magnetron sputtering processes [22,27,28]. The columnar structure gradually disappears after the onset of magnetic shuttering through the upper TiBC layer at approximately one-third of its thickness (Fig. 5a). The 5/55 TiBC layer exhibits a periodic nanolaminated structure with a bilayer period ~4.5 nm, as shown in Fig. 5b. For the 5/55 Ti periodic ratio during 2 h TiBC deposition, the LAFAD Ti source was interrupted 120 times. The top TiBC sub-layer is estimated at ~620 nm, which would result in a theoretical bilayer period thickness of ~5.2 nm, which is fair agreement with the direct measurement in Fig. 5b. When the Ti periodic ratio increases (i.e., 5/25 and 5/15 ratios), the bilayer period thickness decreases to the extent where the nano-layers merge, making the nano-layers difficult to resolve. Increasing the Ti periodic ratio further to the point of continuous Ti deposition should create a quasi-homogenous nanocomposite coating.

Table 3 shows the hardness and Young's modulus of the various top segment TiBC coatings as measured by nanoindentation. Results indicate that Ti modulation by magnetic shuttering can be an effective means of controlling and optimizing hardness with the TiBC 5/25 coating architecture demonstrating a maximum average hardness of 43.2 GPa. Ti modulation was not shown to have a significant effect on Young's modulus

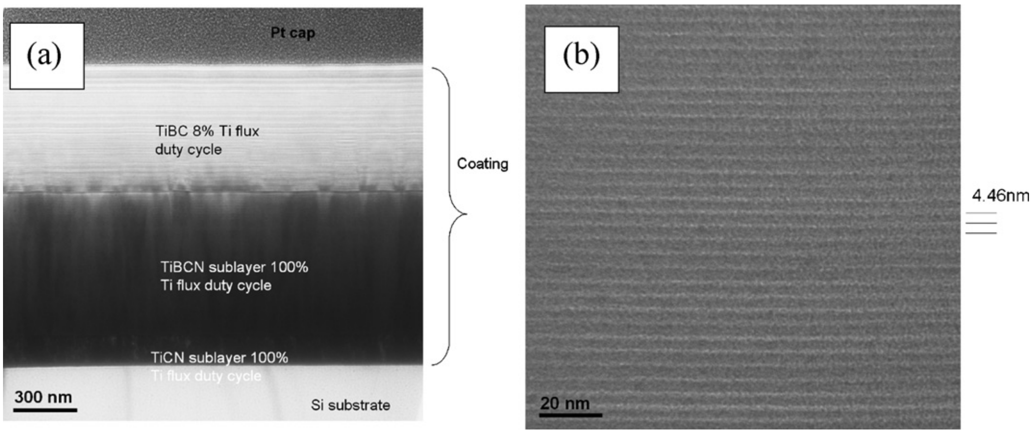

Fig. 5. HRTEM cross-sectional image of a 5/55 TiBC (8% Ti flux duty cycle) top segment nanolaminated architecture: (a) the complete top segment architecture and (b) magnification of the top end of the 5 s/55 s TiBC segment.

Table 3
Mechanical properties of TiBC coatings deposited at different Ti pulse deposition cycles

	Coating (Ti On/Ti Off in s)			
	#1 (0/60)	#3c (5/55)	#2 (5/25)	#5c (5/15)
H (GPa)	37.1	37.0	43.2	39.7
E (GPa)	374	443	455	441
H^3/E^{*2} (GPa)	0.34	0.24	0.36	0.30

which averaged 446 GPa for all periodic ratios, except 0/60 (Ti off) for which the Young's modulus value dropped to 374 GPa. Calculated values of H^3/E^{*2} which are known to be proportional to resistance to plastic deformation and fracture toughness [11–14,31,32] were found to be in the range of 0.24–0.36 GPa. Reported H^3/E^{*2} values from this work are bracketed by work on TiBC films reported at 0.08 GPa and 0.91 GPa deposited by DC unbalanced magnetron sputtering in Refs. [5,33]. In this same work it was found that nitrogen addition to the TiBC(N) architecture could result in high hardness, ~46 GPa, and extremely high H^3/E^{*2} values of ~1.7 GPa [5,33]. Such data would suggest that the current effort using hybrid FAD/UBM techniques may have significant potential to benefit from nitrogen addition used in conjunction with Ti modulation to further control and increase coating toughness while maintaining hardness.

Table 4 shows coating adhesion data as determined by Rockwell C indentation and incremental load (linearly increasing) scratch testing. Rockwell adhesion tests were conducted for

Table 4
Coating adhesion results on Pyrowear 675 and 440A substrates

Coating code	Rockwell C (1450 N)	Scratch test adhesion (N)	
	HF 1–6	L_{c1}	L_{c2}
#1	1–4	52.4	90.3
#2 (1.5 μm TiBC)	1–4	53.7	92.4
#2 (1.0 μm TiBC)	1–4	83.2	91.6
#3c	1	n/a	n/a
#4c	1	35.8	57.5
#5c	1	30.9	43.8

coating #1 and #2 on five separate coated coupons with three tests per coupon. Results were consistent on individual coupons, but scattered for a given architecture, ranging from HF1 (no cracking or delamination) to HF4 (radial cracking and partial delamination) for both coatings #1 and #2. When HF4 results occurred the failure was cohesive at the interface between the TiCrN and TiBC segments. A minimum of three scratch tests on two separate coated P675 coupons were averaged for each coatings #1 and #2, three tests were averaged on one coated 440A coupon for each coating '#3c', '#4c', '#5c'. Coating failure analysis by BEI and SEM imaging provided very accurate determination of initial coating failure, which was termed as the lower critical load (L_{c1}), and described as the point where any partial delamination was apparent. L_{c1} values for coatings #1 and #2 were closely related at ~53 N, and were characterized by partial delamination of the TiBC coating architecture, Fig. 6a, which was consistent with Rockwell adhesion HF4 results.

Additional scratch tests were performed on a thinner TiBC (1 μm) version of coating #2 which showed an increase in the L_{c1} value to 83.2 N. Although not measured, residual stress was presumed to be lower due to decreased coating thickness; the improved adhesion results would seem to indicate that residual stresses in coating #2 play an important role in top segment adhesion. A standard failure load was also observed and described as the point were the TiCrN + TiBC coating was completely removed from the scratch track (L_{c2}) (Fig. 6a). Both coatings #1 and #2 exhibited brittle-coating/brittle-substrate failure modes characterized by mixed compressive spallation and recovery spallation as described by Bull [34]. L_{c2} values were independent of top segment architecture, and driven by the bottom segment coating failure measured consistently at ~91 N (Table 4). Additional scratch tests were performed on coatings #3c, #4c, #5c, as deposited directly onto 440A ductile substrates (HRC 35) without the TiCrN architecture. Both L_{c1} and L_{c2} values were low without the bottom segment present, indicating the importance of residual stress and elastic modulus graduation provided by the TiCrN coating between the substrate and the top segment. More than half of the resulting L_{c1} values corresponded to initial delamination failures at the interface in the top segment between the TiBCN layer and the start of the TiBC magnetically shuttered

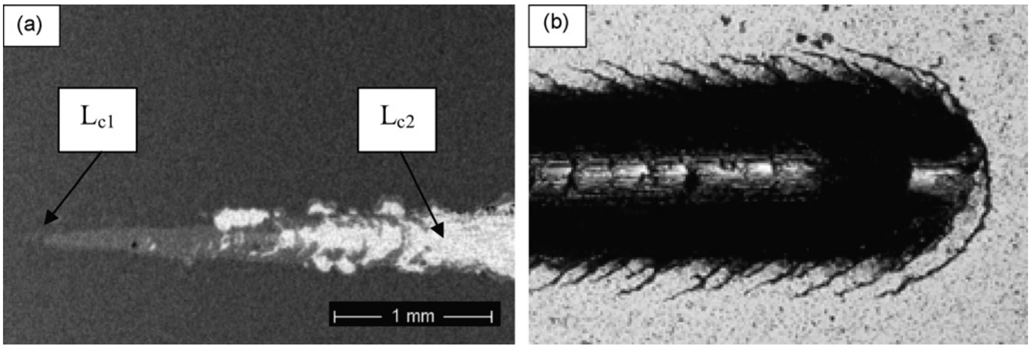

Fig. 6. (a) BEI image of a coating #2 scratch track showing the L_{c1} and L_{c2} values, and the consistent behavior of the TiBC segment (dark gray) to fail prior to the TiCrN segment (light gray, substrate is white). (b) Micrograph of coating #4c scratch track showing the uniform and regular cohesive buckling failure mode observed for TiBC top segment coatings. In both images scratch load increases linearly is from left to right.

layer. Coatings #3c, #4c, #5c also demonstrated very uniform brittle cohesive buckling (through cracks) outside of the scratch track in response to large plastic strains in the 440A substrate (Fig. 6b).

3.1. Sliding wear testing

Lubricated 3.0 GPa contact sliding wear tests were performed for uncoated P675 and for coatings #1 and #2 deposited on P675. To establish basic repeatability two tests were conducted per M50 ball (uncoated)/P675 disc (coated and uncoated) contact pair; wear results were consistent between tests of like contact pairs as maximum wear depths were within 0.25 μm for each test replica. Results for baseline uncoated P675 are shown in Figs. 7 and 10(top). A severe adhesive wear mechanism was evident from profilometry data of the wear scar on the M50 ball counterpart showing large volumes of P675 material transfer when compared with the unworn profile of the ball. Profilometry 3D mapping of uncoated P675 discs showed evidence of adhesive wear coupled with plastic material flow presumably caused by excessive frictional heating of the contact zone. Maximum wear scar depths on uncoated P675 discs averaged 16 μm.

Results for P675 with coating #1 are shown in Figs. 8 and 10(middle). Coating #1 demonstrated mild wear with maximum wear depths averaging 1.5 μm and minor abrasive plowing wear 0.05–0.1 μm deep on the M50 ball counterpart. Maximum wear depths were coincident with the TiCrN bottom segment and TiBC top segment coating interface. Results for P675 coated with coating #2 are shown in Figs. 9 and 10(bottom). Coating #2 demonstrated similar wear performance to coating #1 with maximum wear depths averaging 1.5 μm, and minor plowing wear 0.05–0.1 μm deep (over a less uniform area than coating #1) on the M50 ball counterpart. As with coating #1, maximum wear depths for coating #2 were coincident with the TiCrN bottom and TiBC top segment coating interface. Measured wear scar diameters on both coatings #1 and #2 correlate with calculated Hertzian contact diameters to within 50 μm but a lack of conformal wear on either the M50 balls or the coated P675 discs rules out two and three body abrasion as a primary mechanism. Examination of the 2D wear profiles for coatings #1 and #2 (Figs. 8 and 9) in combination with the top segment coating architecture and thickness information obtained from HRTEM and CALOtest^{TM} data showed a lack of conformal wear, and in all cases wear depths were well correlated to specific interfaces within the coating architecture (primarily the interface between the TiBC–BC and TiBCN layers and the interface between the TiCrN and TiBC segments). From these observations it has been hypothesized that the primary wear mechanism for coatings #1 and #2 is brittle cracking combined with interlayer delamination induced by frictional shear stresses in sliding. This hypothesis is supported by: (1) the propensity of high compressive residual stress coatings to fail at interfaces [35], (2) the nature of the TiCrN + TiBC coatings to exhibit brittle through-cracking as observed in scratch adhesion testing, and (3) preferential wear to coating interface boundaries observed in the direction of frictional shear and extending to the edges of the Hertz contact diameter as shown in Fig. 11.

In comparison with baseline uncoated P675 wear, both coatings #1 and #2 demonstrated 10 times improvement in maximum wear depth and negligible wear to the M50 ball counterpart. The results would suggest further wear resistance could be realized through minimization of the hypothesized brittle fracture and interlayer delamination wear mechanism and transition into steady abrasion mechanisms. Further testing and development is required to determine if this improvement could be realized from a combination of reduction of coating residual stress and improved coating toughness.

3.2. Oil-off testing

As indicated in Section 2, an advanced testing protocol was developed and performed by Wedeven Associates to simulate gas turbine engine bearing operating conditions during an "oil-off" event. Prior development on this testing protocol with uncoated M50 contact pairs and varying turbine engine oils has shown that asperity contact ensues and begins to cause contact zone damage at and above monitored friction values of 0.15. As a result the testing data can be analyzed in two primary ways, the elapsed time of a contact pair to sustain operation in oil-off conditions before a friction value of 0.15 (i.e., contact damage) is reached, and the ability of a contact pair to resist damage during oil-off operation at friction values greater than 0.15 for 200 s.

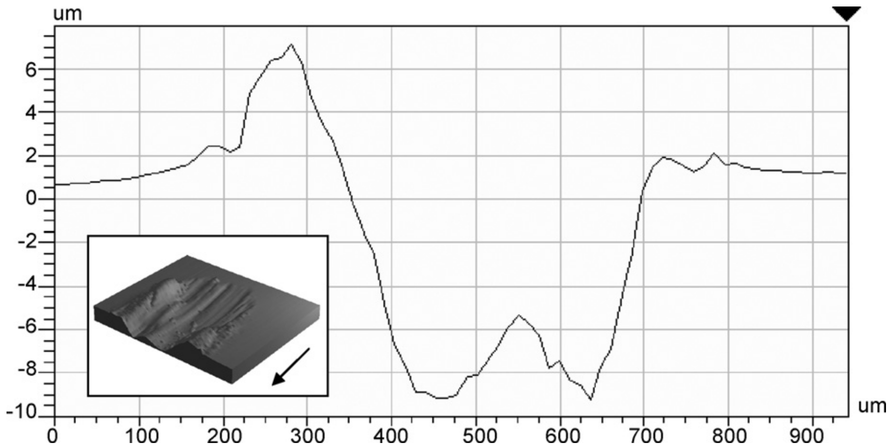

Fig. 7. Cross-section 2D profile of sliding wear test scar on an uncoated Pyrowear 675 disc counterpart, the inset shows a 3D map of the wear scar, the direction of sliding (arrow), and the location of the cross-section. Uncoated Pyrowear 675 discs demonstrated severe adhesive wear and an average maximum wear depth of 16 μm.

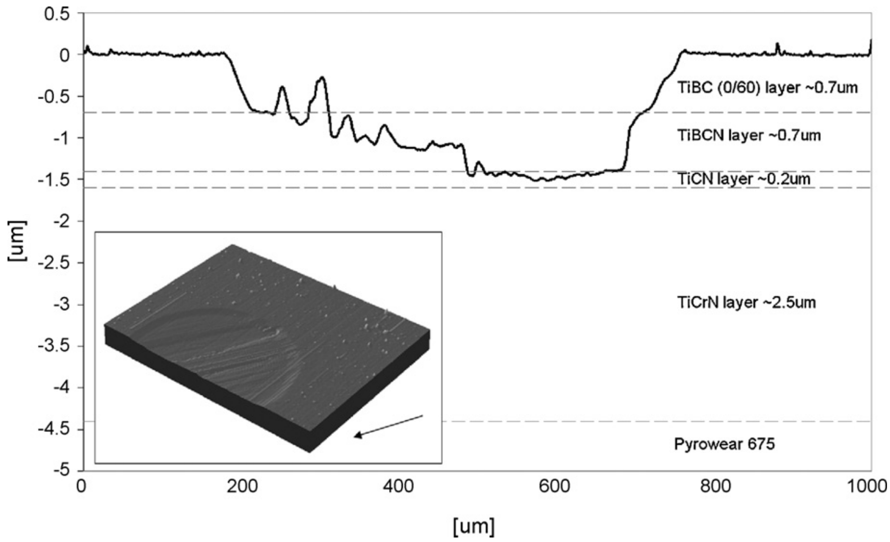

Fig. 8. Cross-section 2D profile of a sliding wear scar on Pyrowear 675 with coating #1, the inset shows a 3D map of the wear scar, the direction of sliding (arrow), and the location of the cross-section. The coating architecture with layer thicknesses is superimposed on the 2D wear scar profile.

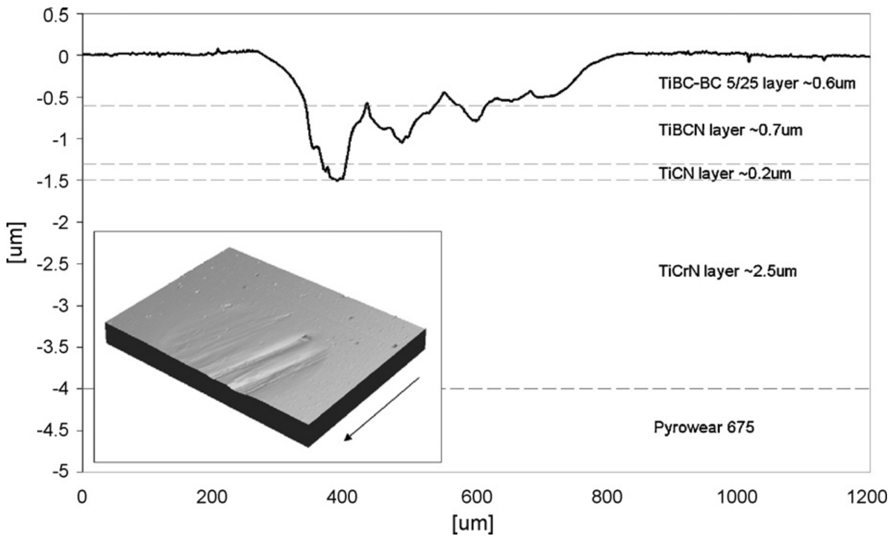

Fig. 9. Cross-section 2D profile of a sliding wear scar on Pyrowear 675 with coating #2, the inset shows a 3D map of the wear scar, the direction of sliding (arrow), and the location of the cross-section. The coating architecture with layer thicknesses is superimposed on the 2D wear scar profile.

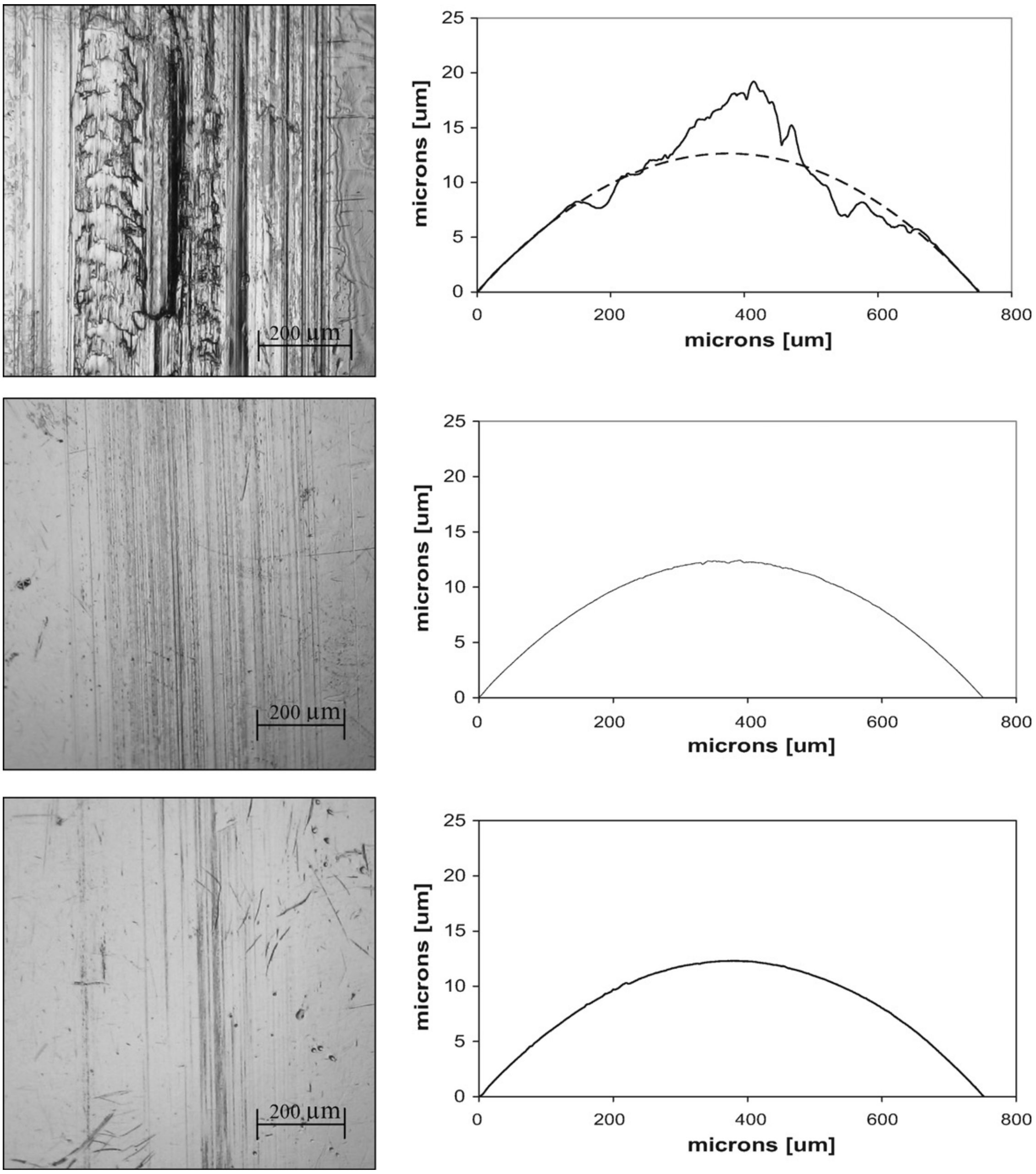

Fig. 10. Micrographs and 2D profiles of sliding wear test scars on uncoated M50 balls vs. uncoated Pyrowear 675 disc (top), Pyrowear 675 disc with coating #1 (middle), and Pyrowear 675 disc with coating #2 (bottom). Severe adhesive wear is evident for contact against uncoated Pyrowear 675 (top) in the 2D profile trace; the dashed line represents the unworn ball profile. Mild plowing abrasion wear, 0.05–0.1 μm deep, was observed on M50 balls in contact with coating #1(middle) and coating #2(bottom), 2D profiles in both cases are nearly identical to the unworn ball.

Table 5
Oil-off protocol test results for various contact pair categories

M50 ball	M50 disc	Average elapsed time to 0.15 friction (s)	Initial steady state EHD friction coeff. (avg)	Friction increase after oil reintroduction (%)
Uncoated	Uncoated	101	0.014	0.032 (132)
Coating #1	Uncoated	31	0.013	0.016 (22)
Coating #2	Uncoated	42	0.016	0.016 (0)
Uncoated	Coating #2	360	0.022	0.029 (34)
Coating #1	Coating #2	425	0.022	0.057 (161)

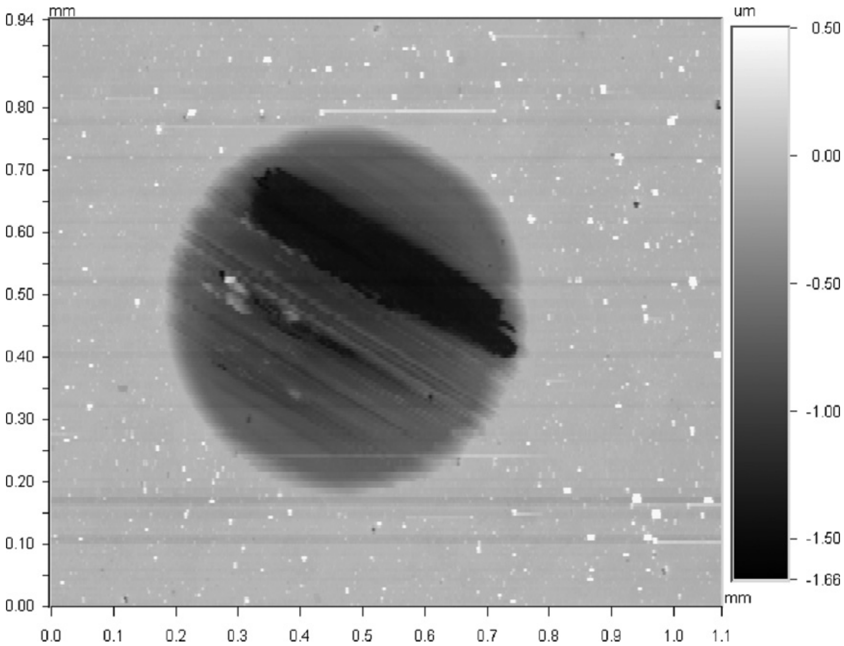

Fig. 11. Profilometry contour plot of sliding wear test scar on Pyrowear 675 with coating #1. Wear in the form of interlayer delamination is evident, induced by brittle through cracking and frictional shear compounded by compressive residual stresses in the coating.

For oil-off testing M50 balls and M50 discs were coated and 10 different contact pair combinations were each tested twice to establish basic repeatability of results. Basic contact pair categories were as follows: uncoated-ball/uncoated-disc (baseline), coated-ball/uncoated-disc, uncoated-ball/coated-disc, and coated-ball/coated-disc. Typical baseline uncoated test results are shown in Fig. 12 are characterized by a short elapsed time to reach a friction coefficient of 0.15. Included in Fig. 12 are typical results for the coated-ball/uncoated-disc contact category which demonstrated a rapid rise to 0.15 friction followed by a friction recovery phase. Table 5 shows average elapsed time to 0.15 friction, initial steady state EHD friction values (prior to oil-off), and recorded percent friction increase after oil reintroduction which indicates relative damaged incurred during the oil-off event.

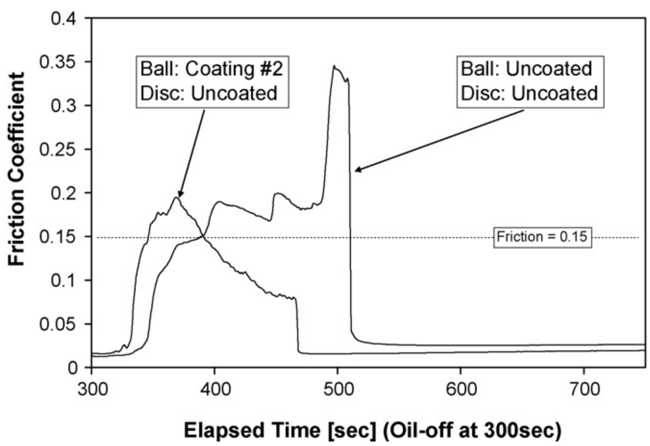

Fig. 12. Friction vs. time plot for oil-off protocol testing of baseline uncoated M50 and coating #2/uncoated-disc contact. Baseline uncoated behavior was characterized by short times to 0.15 friction, followed by what is thought to be sequential boundary lubricant failure/recovery followed by ultimate failure and high >0.3 friction values. Coated ball behavior was characterized by rapid time to 0.15 friction followed by a friction recovery phase until oil reintroduction.

The reduction in contact wear over baseline for the coated-ball/uncoated-disc category is evident in the low percent friction increase data shown in Table 5 and in profilometry maps of the wear tracks shown in Fig. 13. The measured percent friction increase provides an indication of the relative increase in frictional heating that would occur, for example, in high speed bearing systems under which adverse ΔT conditions can cause premature breakdown of lubricants and/or negative bearing clearance leading to severe bearing wear and seizure [36–38]. Both coating #1-ball/uncoated-disc and coating #2-ball/uncoated disc contact categories performed well in this regard demonstrating initial steady state EHD friction values equivalent to baseline uncoated contact, and post-test oil reintroduction EHD friction values that would in actual mechanical operation result in two times less frictional heat generation than uncoated contact pairs.

Test results for uncoated-ball/coated-disc and coated-ball/coated-disc contact pairs were distinctly different than either the baseline or the coated-ball/uncoated disc test results. Contact pairs involving a coating #1-disc did not demonstrate a friction recovery phase, friction plots were similar to baseline and wear was characterized as more severe than baseline uncoated contact. Results for uncoated-ball/coating #2-disc and coating #1-ball/coating #2-disc shown in Fig. 14 and Table 5 were characterized by initial friction spikes to 0.1 after oil-off followed by a long friction recovery phase ending in a rapid rise to high friction values greater than 0.3 for 200 s, and finally a return to EHD friction values after oil reintroduction. Observation of friction data for contact pairs involving a coating #2-disc showed that the groups in question reach a critical failure point

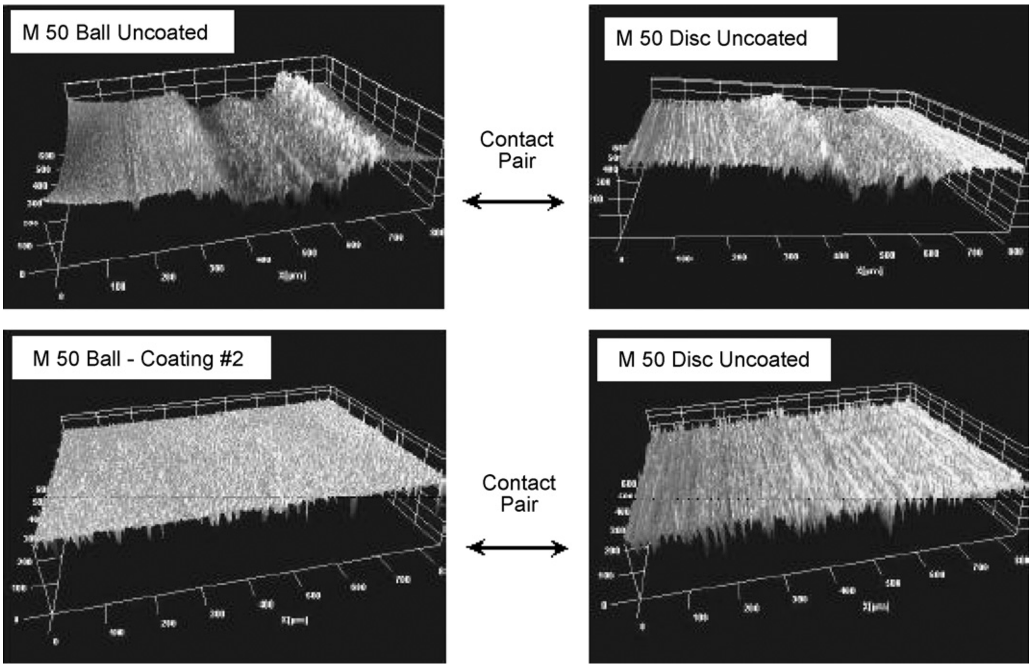

Fig. 13. 3D profilometry surface maps of contact wear for oil-off protocol testing.

where a damage mechanism occurred that caused the friction coefficient to spike above 0.15. Percent increase in friction for uncoated-ball/coating #2-disc and coating #1-ball/coating #2-disc was recorded at 34% and 161%, respectively (baseline: 132%), although observation of the resulting contact track wear by microscopy and profilometry showed that wear in each case was transferred to the ball and was similar or slightly worse in severity to the baseline uncoated case. It is important to note that the developed oil-off protocol calls for 200 s of operation and subsequent reintroduction of oil only after a friction value of 0.15 has been reached. Elapsed time results to reach friction of 0.15 for coating #2-disc pairs averaged 360 s against uncoated-balls,

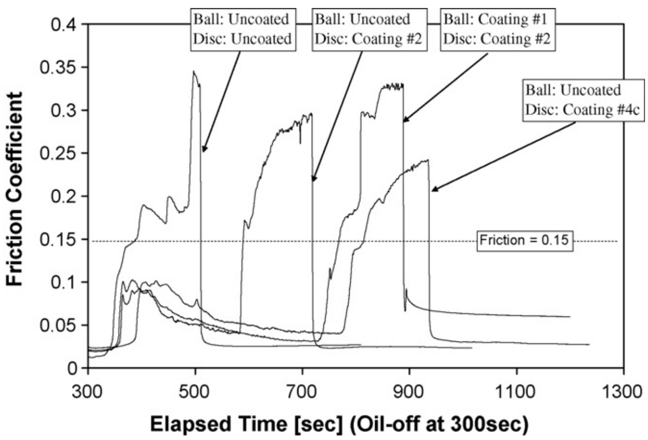

Fig. 14. Friction vs. time plot for oil-off protocol testing of baseline uncoated M50 and contact pairs involving discs with TiBC top segment architectures. A friction recovery phase was observed in 80% of the testing trials, followed by a critical failure point characterized by a rapid rise in friction and subsequent damage to both contact pairs. The duration of the friction recovery phase during oil-off operation ranged from 260 s to 425 s (∼4–7 min) depending on the contact pair.

and 425 s against coating #1-balls, as a result these groups were run in oil-off conditions on average for 1.8–2.0 times as long as the baseline and coated-ball/M50-disc groups. The increase in oil-off test time serves to explain in part the increase in wear observed in coating #2-disc contact pairs, but only if the primary wear mechanism is assumed to be steady.

The concept of non-steady wear and a critical failure point is interesting in this case as the hypothesized brittle-fracture/interlayer-delamination wear mechanism observed in sliding wear testing was observed again in oil-off testing. Fig. 15 shows the observed brittle fracture and delamination behavior on a coating #2-disc and coating #4c-disc; it is important to note that negligible wear was evident in the contact track area outside of the delaminated or fractured areas. A hypothesis under consideration is that the contact pair experiences very little damage in oil-off conditions during the observed friction recovery phase although mechanical support of the coating by the substrate is weakened due to steady contact temperature increase. Current research in scuffing of bulk materials [39,40] emphasizes the occurrence of thermal softening and adiabatic shear failure. As an example, the elastic modulus of M50 decreases from 204 GPa at 27 °C to 127 GPa at 427 °C [41]. In the coated substrate case, local thermal softening of the substrate in the wear track transfers the requirement for resistance to contact zone deformation to the coating, in turn increasing coating tensile strain and the chance of brittle through cracking followed by coating breakup and delamination. The resulting wear debris consisting of delaminated sections of hard coating could easily promote an aggressive wear and friction regime denoted by the critical failure point. The hypothesized behavior could be described as thermally influenced low cycle fatigue failure implying minimal cumulative damage until the critical failure is reached.

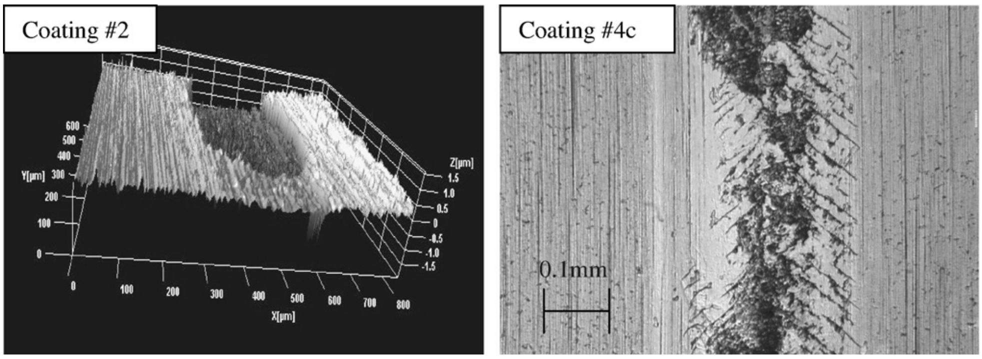

Fig. 15. 3D profile trace of coating #2 and micrograph of coating #4c showing the brittle failure modes observed in oil-off testing. The depth of delamination of coating #2, ∼0.6 μm, indicates failure at the magnetic shuttering interface exposing the TiBCN and bottom segment architectures. Coating #4c (TiBC deposited directly on M50) exhibits brittle through cracking and subsequent breakup. For both coating architectures, wear track areas outside of brittle behavior exhibit mild polishing wear.

From an implementation standpoint the interesting question is whether or not significant cumulative damage occurs in the contact track during the observed friction recovery phase. From an engineering design perspective a well defined coating critical failure mode could be used as an oil-off performance operational limit, for which repeated oil-off events of shorter time could be expected to be managed by a coated contact pair with minimal damage. Standard oil-off testing results for the design of metal/metal commercial aerospace bearings operating at high speeds of 2 MDN (MDN = $10^6 \times$ DN, where DN = inner race diameter (mm) × bearing rev/min) and high loads, demonstrate significant wear after only 15–30 s of oil-off operation and subsequent oil reintroduction [42,43], while current design goals for next generation turbine engine bearings are for higher loads and speeds up to 5 MDN. The ability of coating #2 contact pairs to sustain 360–425 s of oil-off operation versus the baseline time of 103 s in the current oil-off protocol is promising in this regard. More research is needed to understand the observed failure mechanisms, as in the sliding testing conducted; further performance improvements would be expected from coating optimizations that increase coating cohesive toughness.

4. Conclusions

Variations of a dual segment multilayer nanocomposite TiCrN + TiBC coating were successfully deposited on M50 and Pyrowear 675 substrates by LAFAD and hybrid filtered arc/magnetron techniques. Experimental modulation of titanium content within the coating architecture was carried out through precise interruption of titanium entering the chamber by cycling the primary filter coils on and off, a technique termed "magnetic shuttering". HRTEM cross-sectional imaging was used to show that magnetic shuttering was effective in creating well defined nano-layered TiBC–BC architectures, with bi-layer thicknesses on the order of 4.5 nm or less, depending on the periodic Ti flow. Magnetic shuttering was also shown to be an effective means for increasing hardness of the TiBC architectures; hardness values ranged from 37 GPa to 43.2 GPa. The highest hardness and resistance to plastic deformation (H^3/E^{*2}) values were realized for a magnetic shuttering ratio of 5/25 at $H = 43.2$ GPa and $H^3/E^{*2} = 0.36$ GPa, respectively.

Quantitative scratch testing of the coatings demonstrated primarily brittle failure modes, preferential failure at the coating interface between the TiCrN bottom and TiBC top coating segments, and relatively high load values at failure of ∼52 N for the TiBC top segments (cohesive failure) and ∼91 N for the TiCrN bottom segment (adhesive failure). A reduction in top segment coating thickness from 1.5 μm to 1.0 μm caused an improvement in the scratch test cohesive failure load from ∼52 N to ∼83 N, indicating that reduction of compressive residual stress in the coating would likely improve inter-segment cohesion.

High load (3.0 GPa contact stress) boundary lubricated sliding wear testing of the coatings showed an improvement in wear resistance on the order of 10 times over uncoated baseline contact pairs. Uncoated M50 ball bearings in boundary lubricated sliding contact with a coated counterpart demonstrated negligible wear, while uncoated contact pairs demonstrated severe adhesive wear between both counterparts. Cohesive interlayer failure and brittle through cracking were observed to be the primary modes of failure for TiCrN + TiBC coatings.

Simulated turbine engine bearing "oil-off" condition testing was conducted on M50 uncoated/uncoated, coated-ball/uncoated-disc, uncoated-ball/coated-disc, and coated-ball/coated-disc contact pairs. Uncoated/uncoated baseline pairs were characterized by short time to high friction operation and contact pair damage after oil shut-off. Coated-ball/uncoated-disc contact pairs demonstrated rapid rises in friction after oil shut-off, followed by a friction recovery phase resulting in minimal contact pair damage, the best results showing no increase in subsequent EHD friction after 150 s of operation without oil. For certain uncoated-ball/coated-disc and coated-ball/coated-disc contact pairs a low friction operation mode was observed after oil shut-off, during which the contact pair "survived" for up to 425 s without oil before a critical failure mode was reached. The observed critical failure mode for coated contact pairs was thought to be closely related to scuffing failure common to metal/metal contact pairs, in which a rapid rise in friction and damage between the contact pairs occurs. This critical failure mode was hypothesized to be caused by brittle through-cracking of the coating due to increased strain as a result of steadily increasing contact zone temperature, followed by an aggressive abrasive wear regime sustained by hard delaminated coating particles.

Results from the current work indicate that TiBC ternary coatings which are appropriately supported by a coating/substrate architecture system show excellent promise in solving advanced tribological tasks required by sophisticated aerospace mechanical systems. Further research is planned and continued performance improvements are expected with optimizations to TiBC coatings that increase hardness and coating toughness.

Acknowledgements

The authors would like to acknowledge the technical assistance of Recep Avci and Richard Smith at Montana State University. Thanks to Duane Jones for carrying out some of the coating deposition trials. Portions of this research were supported by the United States Department of Defense via the Small Business Innovation Research (SBIR) Program, topic number AF05-181, and managed by Wright Patterson AFB Propulsion Directorate, program manager Dr. Chris Klenke.

References

[1] C.E. Campbell, G.B. Olson, Systems design of high performance stainless steels. I. Conceptual and computational design, J. Comput. Aid. Mater. Des. 7 (2001) 145–170.

[2] M. Jonston, J. Laritz, M. Roads, Thin dense chrome insertion program Pyrowear 675 and cronidar wear testing, Report No. R98AEB240, GE Aircraft Engines Advanced Engineering Program Department, Cincinnati, OH, 1998.

[3] T. Eckhard, K. Bewilogua, G. van der Kolk, T. Hurkmans, T. Trinh, W. Fleischer, Improving tribological properties of sputtered boron carbide coatings by process modifications, Surf. Coat. Technol. 126 (2000) 69–75.

[4] N. Novikov, V.I. Gorokhovsky, B. Uryukov, Superhard I–C coatings used in complex processes of surface strengthening of tools and machine parts, Surf. Coat. Technol. 47 (770) (1991).

[5] I.-W. Park, K.H. Kim, A.O. Kunrath, D. Zhong, J.J. Moore, A.A. Voevodin, E.A. Levashov, Microstructure and mechanical properties of superhard Ti–B–C–N films deposited by dc unbalanced magnetron sputtering, J. Vac. Sci. Technol. B 23 (March/April (2)) (2005) 588–593.

[6] J. Vlcek, S. Potocky, J. Cizhek, J. Houska, M. Kormunda, P. Zeman, V. Perina, J. Zemek, Y. Setsuhara, S. Konuma, Reactive magnetron sputtering of hard Si–B–C–N films with a high-temperature oxidation resistance, J. Vac. Sci. Technol. A 23 (November/December (6)) (2005) 1513–1523.

[7] R. Hauret, J. Patscheider, From alloying to nanocomposites—improved performance of hard coatings, Adv. Eng. Mater. 2 (2000) 247–259.

[8] P.Y. Yashar, W.D. Sproul, Nanometer scale multilayered hard coatings, Vacuum 55 (1999) 179–190.

[9] K. Bewilogua, C.V. Cooper, C. Specht, J. Schroder, R. Wittorf, M. Grischke, Effect of target material on deposition and properties of metal-containing DLC (Me-DLC) coatings, Surf. Coat. Technol. 127 (2000) 224–232.

[10] P. Karankova, M.G.J. Veprek-Heijman, O. Zindulka, A. Bergmaier, S. Veprek, Superhard nc-TiN/a-BN and nc-TiN/a-TiB_x/a-BN coatings prepared by plasma CVD and PVD: a comparative study of their properties, Surf. Coat. Technol. 163–164 (2003) 149–156.

[11] S. Zhang, D. Sun, Y. Fu, H. Du, Recent advances of superhard nanocomposite coatings: a review, Surf. Coat. Technol. 198 (2005) 2–8.

[12] P.Eh. HovsepianU, D.B. Lewis, W.-D. Munz, Recent progress in large scale manufacturing of multilayer superlattice hard coatings, Surf. Coat. Technol. 133–134 (2000) 166–175.

[13] J. Musil, Hard nanostructured and nanocomposite thin films, in: Proceedings of the Third Mikkeli International Industrial Coating Seminar MIICS-2006, Mikkeli, Finland, March 16–18, 2006.

[14] A. Leiland, A. Matthews, On the significance of the *H*/*E* ratio in wear control: a nanocomposite coating approach to optimised tribological behavior, Wear 246 (2000) 1–11.

[15] A.A. Voevodin, S.D. Walck, J.S. Zabinski, Architecture of multilayer nanocomposite coatings with super-hard diamond-like carbon layers for wear protection at high contact loads, Wear 203–204 (1997) 516–527.

[16] A.A. Voevodin, J.S. Zabinski, Load-adaptive crystalline/amorphous nanocomposites, J. Mater. Sci. 33 (1998) 319–327.

[17] A.A. Voevodin, J.P. O'Neill, J.S. Zabinski, Nanocomposite tribological coatings for aerospace applications, Surf. Coat. Technol. 116–119 (1999) 36–45.

[18] A.A. Voevodin, J.S. Zabinski, Supertough wear resistant coatings with 'chameleon' surface adaptation, Thin Solid Films 370 (2000) 223–231.

[19] A.A. Voevodin, M.A. Capano, S.J.P. Laube, M.S. Donley, J.S. Zabinski, Design of a Ti/TiC/DLC functionally gradient coating based on studies of structural transitions in Ti–C films, Thin Solid Films 298 (1997) 107–115.

[20] A.A. Voevodin, J.S. Zabinski, Nanocomposite and nanostructured tribological materials for space applications, Compos. Sci. Technol. 65 (2005) 741–748.

[21] H.W. Wang, M.M. Stack, S.B. Lyon, P. Hovsepian, W.-D. Munz, Wear associated with growth defects in combined cathodic arcrunbalanced magnetron sputtered CrNrNbN superlattice coatings during erosion in alkaline slurry, Surf. Coat. Technol. 126 (2000), 279-287 72.

[22] N.J.M. Carvalho, Ph.D. Thesis, Rijksuniversiteit Groningen, 2001, ISBN 90 367.

[23] V.I. Gorokhovsky, R. Bhattacharya, D.G. Bhat, Characterization of large area filtered arc deposition technology. Part I. Plasma processing parameters, Surf. Coat. Technol. 140 (2) (2001) 82–92.

[24] V.I. Gorokhovsky, D.G. Bhat, R. Bhattacharya, A.K. Rai, K. Kulkarni, R. Shivpuri, Characterization of large area filtered arc deposition technology. Part II. Coating properties and applications, Surf. Coat. Technol. 140 (3) (2001) 215–224.

[25] V. Gorokhovsky, US Patent No. 6,663,755.

[26] V. Gorokhovsky, C. Bowman, P. Gannon, D. Van Vorous, A. Voevodin, A. Rutkowski, C. Muratore, R.J. Smith, A. Kayani, D. Gelles, V. Shutthanandan, B.G. Trusov, Tribological performance of hybrid filtered arc–magnetron coatings. Part I. Coating deposition process and basic coating properties characterization, Surf. Coat. Technol. 201 (6) (2006) 3732–3747.

[27] V. Gorokhovsky, C. Bowman, P. Gannon, D. VanVorous, A. Voevodin, A. Rutkowski, Tribological performance of hybrid filtered arc–magnetron coatings. Part II. Coating deposition process and basic coating properties characterization, Surf. Coat. Technol. 201 (14) (2007) 6228–6238.

[28] V. Gorokhovsky, B. Heckerman, P. Watson, N. Bekesch, The effect of multilayer filtered arc coatings on mechanical properties, corrosion resistance, and performance of periodontal dental instruments, Surf. Coat. Technol. 200 (18–19) (2006) 5614–5630.

[29] R.J. Smith, C. Tripp, A. Knospe, C.V. Ramana, A. Kayani, V. Gorokhovsky, V. Shutthanandan, D.S. Gelles, Using CrAlN multilayer coatings to improve oxidation resistance of steel interconnects for solid oxide fuel cell stacks, J. Mater. Eng. Perform. 13 (2003) 295.

[30] H. Jehn, G. Reiners, N. Siegel, DIN-Fachbericht (special report) 39, Charakterisierung duenner Schichten (Characterization of Thin Layers), Beuth-Verlag, Berlin, 1993.

[31] J. Musil, F. Kurn, H. Zeman, H. Polakova, Relationships between hardness, Young's modulus and elastic recovery in hard nanocomposite coatings, Surf. Coat. Technol. 154 (304) (2002).

[32] M. Stoiber, S. Perlot, C. Mitterer, M. Beschliesser, C. Lugmair, R. Kullmer, PACVD TiN/Ti–B–N multilayers: from micro- to nano-scale, Surf. Coat. Technol. 177 (348) (2004).

[33] Shtansky, V. Dmitry, Moore, J. John, Levashov, A. Evgeny, Voevodin, A. Andrey, Nanostructured thin films and nanodispersion strengthened coatings, NATO Sci. Series II: Math. Phys. Chem. 155 (2004).

[34] S.J. Bull, Failure modes in scratch adhesion testing, Surf. Coat. Technol. 50 (1991) 25–32.

[35] M.D. Drory, J.W. Hutchison, Measurement of the adhesion of a brittle film on a ductile substrate by indentation, Proc. Roy. Soc. London A 452 (1996) 2319–2341.
[36] S. Ijuin, et al., STLE, Tribol. Trans. 38 (2) (1995) 403–409.
[37] S. Lacey, H. Kawamura, Motion & Control No. 5, NSK-RHP European Tech Centre, 1998.
[38] A. Dodd, N. Mitamura, H. Kawamura, Motion & Control No. 6, 1999.
[39] J. Hershberger, O.O. Ajayi, J. Zhang, H. Yoon, G.R. Fenske, Evidence of scuffing initiation by adiabatic shear instability, Wear 258 (2005) 1471–1478.
[40] M.R. Staker, The relationship between adiabatic shear instability strain and material properties, Acta Metall. 29 (1981) 683–689.
[41] Timken Latrobe Steel, Data Sheet: Lescalloy M50 Vim-Var, 2005, www.timkenlatrobe.com.
[42] L. Wang, R.W. Snidle, L. Gu, Wear 246 (2000) 159–173.
[43] Y. Shoda, S. Ijuin, H. Aramaki, H. Yui, K. Toma, Tribol. Trans. 40 (4) (1997) 684–767.
[44] N.A. Vatolin, G.K. Moiseev, B.G. Trusov, Thermodynamic Modeling in High Temperature Inorganic Systems, Metallurgy, Moscow, 1994 (in Russian).
[45] A.I. Gusev, A.A. Rempel, A.J. Magerl, Disorder and Order in Strongly Non-Stoichiometric Compounds, Springer, 2001, p. 607.
[46] H. Duschanek, P. Rogl, H.L. Lukas, A critical assessment and thermodynamic calculation of the boron–carbon–titanium (B–C–Ti) ternary system, J. Phase Equilib. 16 (1995) 46–60.
[47] P. Rogl, H. Bittermann, Ternary metal boron carbides, Int. J. Refract. Met. Hard Mater., 17 (1–3) (1999) 27–32.
[48] E. Amberger und, H.P. Gerster, Struktur ternärer *I*-tetragonaler boride: $(B_{12})_4C_2Ti_{1.86}$ und $(B_{12})_4C_2V_{1.29}$, Acta Crystallogr. B 36 (1980) 672–675.